ES Energy & Environment

RESEARCH PAPER View Article Online

Thermoelectric Properties of Hexagonal WN_6 from First-Principles Calculations

Xueliang Zhu,[1] Pengfei Liu,[2,3] Hao Gao,[8] Guofeng Xie[4,5*] and Baotian Wang[2,3,6,7*]

Recent research demonstrated high thermoelectric figure of merit in CrN, implying that the transition metal nitrides could be promising thermoelectric materials. Herein, we investigate the thermoelectric properties of a newly predicted superhard material WN_6 by using first-principles calculations and Boltzmann transport theory. Results indicate that WN_6 has a small band gap of 0.76 eV, a relatively low lattice thermal conductivity of around 10.7 W/mk at 700 K, and a large Seeback coefficient of 1330 μV/K at 300 K. Its low lattice thermal conductivity and large Seeback coefficient lead to an excellent thermoelectric response, with the maximum thermoelectric figure of merit being 0.78 for n-type. The mode Grüneisen parameters and phonon mean free path are exhibited to analyze the anharmonic properties and the size effects. These results shed light on the thermoelectric performance of WN_6.

Keywords: Transition metal nitrides; Thermoelectric; Phonon transport; First-principles calculations

Received 12 November 2018**, Accepted** 20 December 2018

DOI: 10.30919/esee8c213

1. Introductions

Thermoelectric materials, can directly convert thermal energy into electrical energy, play an important role in sustainable energy future.[1-6] However, the conversion efficiency of thermoelectric devices is relatively low on account of their limitations measured through the thermoelectric figure of merit (*ZT*),[7,8]

$$ZT=S^2\sigma T/\kappa, \quad (1)$$

where S is the Seebeck coefficient, σ is the electronic conductivity, T is the absolute temperature, and κ is the thermal conductivity, respectively. The κ can be divided into the lattice thermal conductivity κ_l and the electronic thermal conductivity κ_e. To search a new material with a high *ZT*,[9-14] a combination of low thermal conductivity and high Seebeck coefficient is desired.[15,16] However, optimizing one parameter without affecting another is extremely difficult due to the complex competing between them.

In the past decade, several approaches to enhance the *ZT* have been applied, including the band structure engineering,[17] electron energy barrier filtering,[18] quantum confinement effects,[19] nanostructuring,[20,] and phononic crystal patterning.[21-24] Searching for new materials with intrinsically low thermal conductivity is another path. The most common pristine thermoelectric materials are IV-VI (SnSe,[25] Bi_2Te_3,[26] PbTe,[27] PbSe[28]) semiconductors, all of which possess a fairly low lattice thermal conductivity. Various other materials, such as silicides,[29] skutterudite,[30] clathrates,[31] sulfides[32] and transition metal nitrides,[33] also exhibit bad phonon transport properties. For transition metal nitrides, their high hardness, excellent electronic properties, good thermal stability, and high melting point endow them as good thermoelectric materials. For example, CrN has been synthesized and reported to be a promising n-type thermoelectric material with an abnormally low lattice thermal conductivity (3.8 W/mk) and a high *ZT* value of 0.12 at room temperature.[34]

Recently, several tungsten nitrides with stoichiometries of WN, WN_2, W_2N_3,[35] W_3N_4[36] and WN_6[37] have been found in the W-N systems. Among them, WN_6 was reported being a semiconductor while the others are semimetals or metals. The newly predicted hexagonal phase of WN_6 has an indirect band gap (0.76 eV), exotic electronic structure, high melting point of ~1900 K, good volumetric (28.0 kJ/cm^3) and ultra-high hardness (57 GPa). Although this structure could be only synthesized at high pressure of around 65 GPa, it is quenchable to ambient pressure.[37] Considering all these merits for this material, it is greatly valuable to investigate its thermoelectric properties.

In the present work, by using first-principles calculations and Boltzmann transport theory, we systematically study the thermoelectric properties of the superhard WN_6. We find that its maximum *ZT* value of 0.78 can be achieved for the n-type case, indicating that WN_6 could be a promising material for thermoelectric applications. A low lattice thermal conductivity and a large Seebeck coefficient are responsible for this

[1]*School of Physics and Optoelectronics, Xiangtan University, Hunan 411105, China*
[2]*Institute of High Energy Physics, Chinese Academy of Sciences (CAS), Beijing 100049, China*
[3]*Dongguan Neutron Science Center, Dongguan 523803, China*
[4]*School of Materials Science and Engineering, Hunan University of Science and Technology, 411201 Xiangtan, China.*
[5]*Hunan Provincial Key Lab of Advanced Materials for New Energy Storage and Conversion, 411201 Xiangtan, China*
[6]*Institute of Applied Physics and Computational Mathematics, Beijing 100088, China*
[7]*Collaborative Innovation Center of Extreme Optics, Shanxi University, Taiyuan, Shanxi 030006, China*
[8]*National Laboratory of Solid State Microstructures, School of Physics and Collaborative Innovation Center of Advanced Microstructures, Nanjing University, Nanjing 210093, China*
***E-mail:** gfxie@xtu.edu.cn; wangbt@ihep.ac.cn*

result. The size effect is also analyzed by calculating its cumulative thermal conductivity.

2. Methods

First-principles calculations are performed by using the Vienna *ab*-initio simulation package[38] based on density Functional theory (DFT). The Perdew-Burke-Ernzerh (PBE)[39] functional form of the generalized gradient approximation is adopted to describe the exchange and correlation effects. The kinetic-energy cutoff of the plane-wave basis is chosen as 800 eV. The Brillouin zone (BZ) of the primitive cell is sampled by a Monkhorst-Pack *k*-mesh of 11 × 11 × 11. The geometric structure is fully relaxed until the residual forces on atoms are less than 0.01 eV/Å. The total energy convergence is set as 10^{-6} eV/Å.

The phonon transport properties are calculated from the Boltzmann transport equation as implemented in the ShengBTE code,[40] in which the harmonic second-order interaction force constants (2nd IFCs) and the anharmonic third-order IFCs (3rd IFCs) are used as input. The 2nd IFCs and phonon dispersions are calculated by using the PHONONPY package[41] with the supercell approach. A 2 × 2 × 2 supercell with 5 × 5 × 5 *k*-mesh is used. The 3rd IFCs, reflecting the properties of the phonon-phonon scatting, are calculated using same size of supercells with the finite-difference method.[42] The interactions including the sixth-nearest-neighbor atoms are taken into account for the 3rd IFCs. After testing the convergence of the k-grid in calculating the lattice thermal conductivity (figure S1, supplementary material), a dense 11 × 11 × 11 *k*-mesh is used.

The electronic transport properties are calculated using semi-classical Boltzmann transport theory and the rigid band approach as implemented in the BoltzTrap code.[43] The constant relaxation time approximation is applied, which is valid when the relaxation time does not vary strongly with the energy scale of k_BT. This approximation has verified the thermoelectric properties of many materials accurately.[44-48] Dense 35 × 35 × 35 *k*-mesh is used in the BZ to enable accurate Fourier interpolation of the Kohn−Sham eigenvalues.

3. Results and Discussions

3.1 Atomic and electronic structures

In Fig. 1, we show the crystal structure of the hexagonal WN_6. It crystallizes in the $R\bar{3}m$ (166) space group with three formula units (f.u.) in its conventional unit cell. There is only one f.u. in its primitive rhombohedral cell. Interestingly, the WN_6 is composed of tungsten atoms and armchair-like N_6 rings (Figs. 1b and 1c). From the side, the WN_6 looks like a layer structure. The relaxed hexagonal lattice constants are a=6.152 Å and c=4.562 Å, with the bond distances of W-N and N-N being 2.29 Å and 1.45 Å, respectively. The detailed structure parameters are consistent with the previous theoretical reports.[37] Here, the *a*, *b* and *c* axis correspond to the *x*, *y* and *z* directions, respectively.

We present the orbital-resolved band structure and corresponding electronic density of states (DOS) of WN_6 in Figs. 2a and 2b. Obviously, the WN_6 is a semiconductor with the valence band maximum (VBM) and the conduction band minimum (CBM) locating at Z and L points, respectively. The band gap is calculated to be 0.76 eV. In the vicinity of Fermi level, the valence band (VB) is mainly occupied by the N-2*p* orbitals, whereas the conduction band is primarily contributed by the W-5*d* orbitals. A mixture of light and heavy bands can be observed over the VB. Specifically, the light band around the Z point can provide high electronic mobility and electronic conduction while the heavy band at L point is beneficial for good Seebeck coefficients.[49-52] The DOS fully reflects the contribution of the atomic orbitals, which is consistent with the orbital-resolved band structure. We observe that there is almost no contribution from the W-6*s* orbitals.

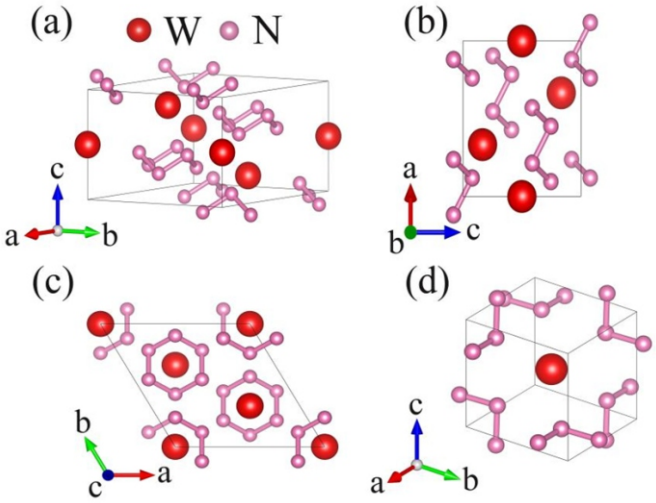

Fig. 1 (a) Hexagonal crystal structure; **(b)-(c)** side and top views of the conventional cell; and **(d)** primitive cell of WN_6.

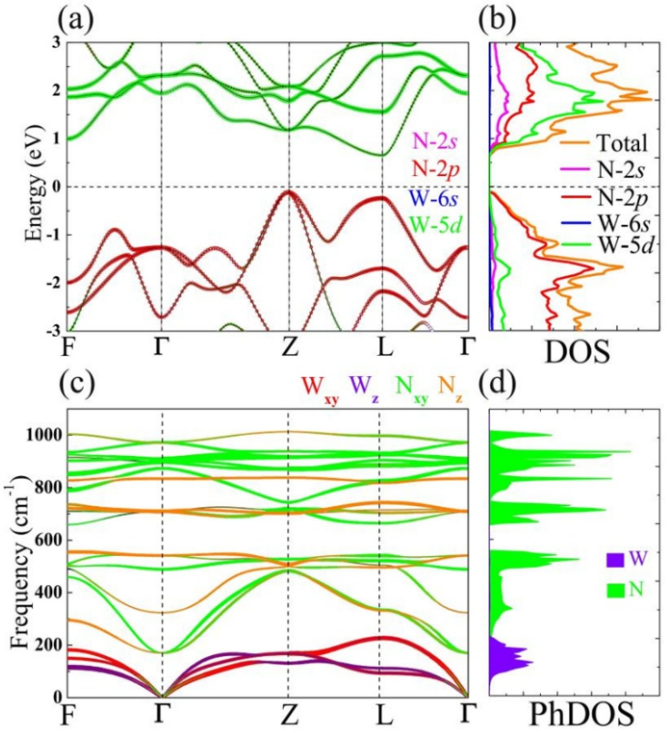

Fig. 2 (a) Orbital-resolved band structure, **(b)** partial and total DOS, **(c)** phonon dispersions, and **(d)** partial-atoms PhDOS of WN_6.

3.2 Phonon transport properties

We first validate the phonon dispersion curves of WN_6, which is calculated by solving the eigenvalues of the harmonic IFCs matrix. The phonon dispersion curves with their color weighted by the contributions of N and W atoms are calculated to guarantee the optimized structure locating at the minimum on potential energy surface (Fig. 2c). We find that the hexagonal WN_6 is dynamically stable at ambient pressure, as

indicated by the positive phonon frequencies. There exist three acoustic and eighteen optical phonon branches corresponding to the seven atoms primitive cell of WN_6. Meanwhile, the phonon dispersion curves can be divided into two portions, the low frequency acoustic phonon branches region (< 200 cm^{-1}) and the high frequency optical branches region (> 200 cm^{-1}). From the decomposition of the phonon curves with respect to W and N atomic vibrations as well as the corresponding projected phonon density of states (PhDOS), it is clear that the acoustic phonon branches mainly contain the W atomic vibration while the vibrations of N atoms dominate on all the optical modes (Figs. 2c and 2d). The lowest frequency of the optical branch is located at the Γ point (170 cm^{-1}). Near this point, a large concave appears (see the blue rectangle region) in frequency range of 170 to 500 cm^{-1}. To study the lattice thermal conductivity, we firstly analyze the phonon group velocities v, $v = \frac{d\omega(\boldsymbol{q})}{d\boldsymbol{q}}$, and plot them in Fig. 3b. Much large values of the v can be seen in frequency range of 170 to 500 cm^{-1}, corresponding to phonons in the blue rectangle region in Fig. 2c. After arithmetic averaging, we obtain the average v to be 1.3 km/s. The average v for the first three optical modes along the F-Z direction of about 4.1 km/s is greatly larger than the whole one.

The lattice thermal conductivity is calculated using the self-consistent iterative approach as below:

$$\kappa_{l,\alpha\beta} = \Sigma_{\boldsymbol{q}\lambda} C_V(\boldsymbol{q}\lambda) v^{\alpha}(\boldsymbol{q}\lambda)\, v^{\beta}(\boldsymbol{q}\lambda)\tau_{\boldsymbol{q}\lambda}, \quad (2)$$

where C_V is the phonon model specific heat, v^{α} is the phonon group velocity along α direction, and $\tau_{q\lambda}$ is the phonon relaxation time of phonon mode of wave vector $\boldsymbol{q}$ and branch index λ. The lattice thermal conductivities are calculated to be 26.4 and 29.6 W/mk along *xx* and *zz* directions at room temperature, respectively. The small difference between the thermal conductivity along *xx* and *zz* directions is due to the weakly anisotropy of the phonon group velocities (figure S2, supplementary material). According to the contribution of κ_l (fig. S3 in the supplementary material), one can see that the contribution to the κ_l is mainly from the acoustic phonon branches. Therefore, the W atoms play the dominant role in the thermal transport. In Fig. 3a, we plot the κ_l of WN_6 along *xx* and *zz* directions as a function of temperature. From our present results, we can see clearly the rapid decreasing behavior of the κ_l of WN_6 in temperature range from 200 K to about 500 K. Above temperature of 500 K, the decrease behavior is slow down and the κ_l tends to a constant value upon heating furtherly. This phenomenon mainly originates from the intrinsic enhancement of the phonon-phonon scattering.

In order to gain more information of the thermal properties, we calculate the phonon relaxation time and the Grüneisen parameters and present them in Figs. 3c and 3d. At room temperature, the average relaxation time of the acoustic modes is about 21 ps, about five times of the optical modes. In addition, the phonon relaxation time of the two transverse acoustic modes (TA_1 and TA_2) is longer than that of the longitudinal acoustic (LA) mode, indicating that the contribution to the κ_l from the TA_1 and TA_2 is larger than that from the LA mode. The mode Grüneisen parameters are calculated according to

$$\gamma_{\lambda}(\boldsymbol{q}) = -\frac{\alpha_0}{\omega_{\lambda}(\boldsymbol{q})} \frac{\partial\omega_{\lambda}(\boldsymbol{q})}{\partial_{\alpha}}, \quad (3)$$

where α_0, λ, and $\boldsymbol{q}$ represent the equilibrium lattice constant, phonon branch and wave vector respectively. They can be used to quantify the anharmonic interactions. Usually, large γ indicates strong anharmonicity. The largest γ of about 4.8 appears on the TA_1 branch, which would greatly suppress the phonon transport in the high temperature region. The average Grüneisen parameter is about 1.2, manifesting a moderate anharmonic phonon scattering.

Nanostructuring is one major approach for ZT enhancement, since it effectively hinders phonon transport and has little effect on electron transport.[53-61] If the size of device is as small as the phonon mean free path (MFP), the lattice thermal conductivity would be significantly depressed by the frequent phonon-surface scattering. Therefore, knowledge of MFP is essential to understanding size effects and designing nanoscale thermoelectric devices.[62-66] Herein, we get the characteristic MFP at temperature T by fitting the cumulative thermal conductivity as a single parametric function.[40]

$$\kappa(l) = \frac{\kappa_{max}}{1+\frac{l_0}{l}} \quad (4)$$

where κ_{max} is the ultimate thermal conductivity, l_0 is the evaluated characteristic phonon MFP. The cumulative thermal conductivity of WN_6 at different temperature is shown in Figs. 3e and 3f. The cumulated κ_l keeps increasing as l increases, until reaching the thermodynamic limit. For the l_0 values, we find 66 nm, 32 nm and 15 nm for the *xx* direction at 300, 500 and 700 K, and for the *zz* direction, the l_0 is 63 nm, 31 nm and 15 nm, respectively. The difference of l_0 along *xx* direction and along *zz* direction is small, especially at high temperature. This is consistent with the weak anisotropy of κ_l shown in Fig 3a. Researching the MFP of WN_6 will be beneficial to analyze the size effect on ballistic or diffusive phonon transport and further improve the thermoelectric properties.

3.3 Electrical transport properties

Using the semi-classical Boltzmann transport theory based on the rigid band approach, we investigate the electrical transport properties. Since the scattering time is difficult to calculate, a constant value is employed in this work. The negative and positive μ correspond to p and n-type, respectively. The transport coefficients as functions of temperature and chemical potential μ can be calculated using the Fermi-Dirac distribution function f_{μ},[43]

$$\sigma_{\alpha\beta}(T,\mu) = \frac{1}{V}\int \Sigma_{\alpha\beta}(\epsilon)\left[-\frac{\partial f_{\mu}(T,\epsilon)}{\partial\epsilon}\right] d\epsilon, \quad (5)$$

$$S_{\alpha\beta}(T,\mu) = \frac{1}{eTV\sigma_{\alpha\beta}(T,\mu)}\int \Sigma_{\alpha\beta}(\epsilon)\,(\epsilon-u)\left[-\frac{\partial f_{\mu}(T,\epsilon)}{\partial\epsilon}\right] d\epsilon, \quad (6)$$

where α and β are Cartesian indices, V is the volume of the primitive cell, e is the charge of an electron, and $\Sigma_{\alpha\beta}(\epsilon)$ is the transport distribution function.

Figs. 4a and 4b show the Seebeck coefficients for the *xx* and *zz* directions as a function of chemical potential at different temperatures. Obviously, the WN_6 exhibits relatively large values of the Seebeck coefficients with weak anisotropy. The Seebeck coefficient of the n-type is slightly higher than that of the p-type. At room temperature, the maximum Seebeck coefficient in n-type can reach to 1310 μV/K and 1330 μV/K along *xx* and *zz* directions, respectively. Such large Seebeck coefficients of WN_6 are beneficial for the thermoelectric applications. The temperature-dependent decreasing behavior of the Seebeck coefficients is slowing down along with increasing the temperature. This phenomenon is a typical behavior of thermoelectric materials and

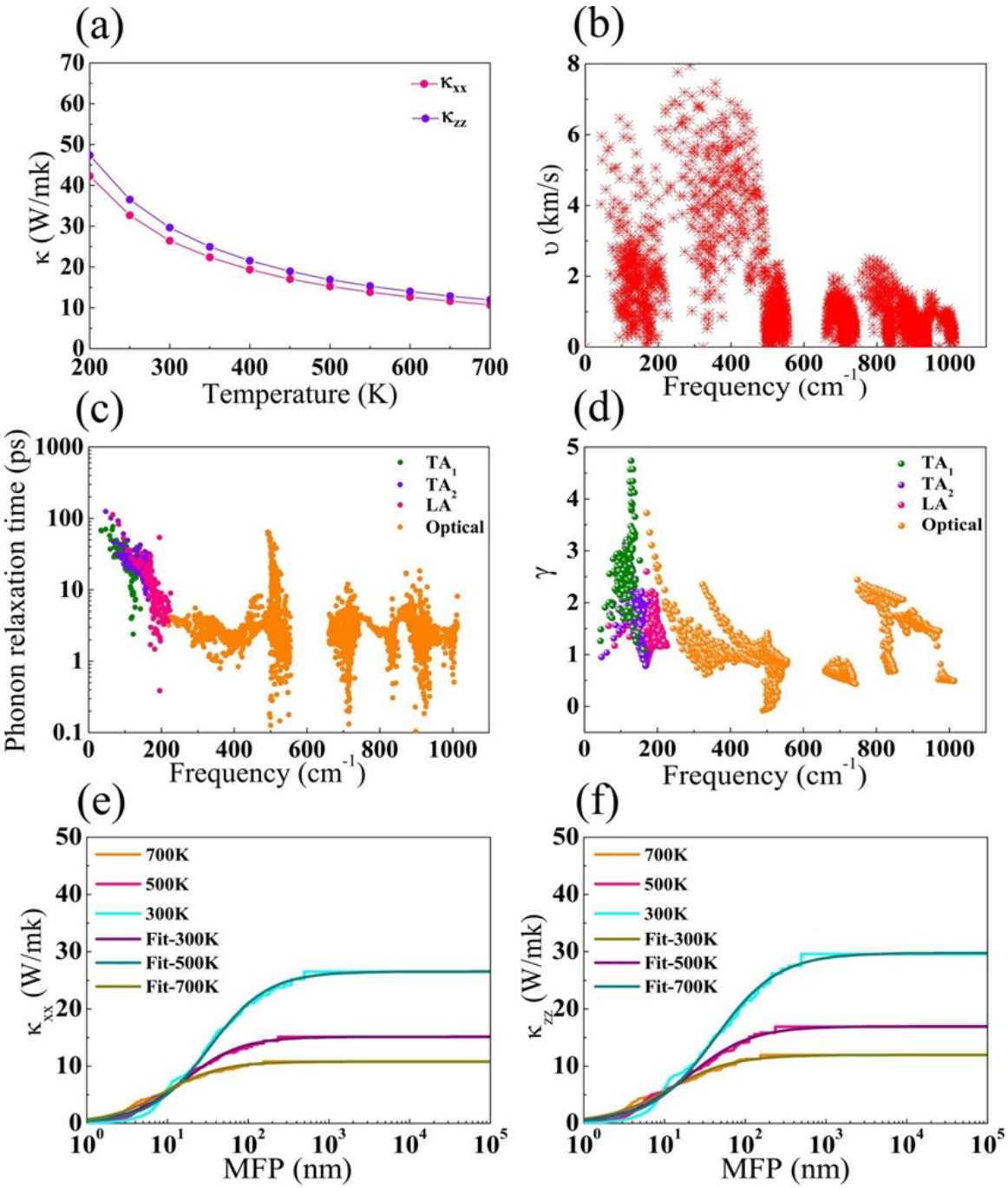

Fig. 3 (a) Temperature dependence of lattice thermal conductivity along the directions of *xx* and *zz*. Frequency dependences of **(b)** phonon group velocities, **(c)** phonon relaxation time, and **(d)** mode Grüneisen parameters. Cumulative lattice thermal conductivity of WN_6 as a function of the phonon MFP at 300, 500 and 700 K along **(e)** *xx* and **(f)** *zz* directions.

depends on their band gap.[67,68] At low chemical potential, we can see that the Seebeck coefficients appear peaks due to electron transition from valence bands to conduction bands as shown in Fig. 2a.

Figs. 4c and 4d show the electrical conductivity σ/τ as a function of chemical potential. We can see that the hexagonal WN_6 displays a relatively high electrical conductivity with weakly anisotropic. The temperature has a weak effect on electrical conductivity. In addition, the σ/τ of n-type along the *xx* direction is smaller than that along the *zz* direction, while in the p-type case its value along the *xx* direction is larger than that along the *zz* direction in μ-range of -1 eV to 1 eV. This can be qualitatively understood from the different electronic energy bands along the *xx* and *zz* directions. Our calculated results show that n-type of WN_6 has a good performance of electrical conductivity.

The κ_e with respect to the scattering time is shown in Figs. 4e and 4f by solving the Wiedemann-Franz law[69]

$$\kappa_e = L\sigma T \tag{7}$$

where $L=\pi^2\kappa_B^2/3e^2$ is the Lorenz number, κ_B is the Boltzmann constant, σ is the electrical conductivity. Similar to the electrical conductivity, the κ_e

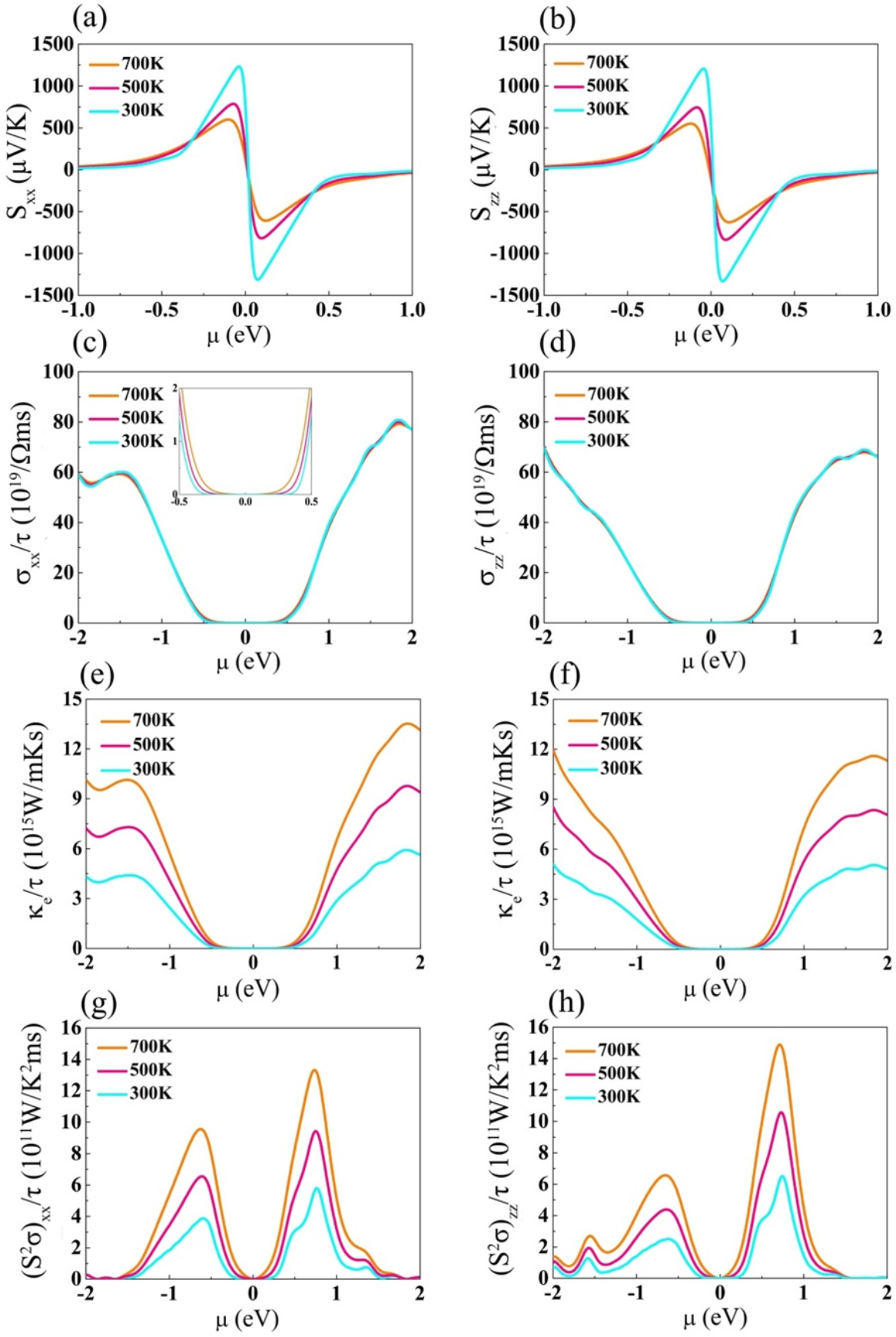

Fig. 4 (a)-(h) Seebeck coefficients (first layer), electrical conductivity with respect to the scattering time (second layer), electronic thermal conductivity with respect to the scattering time (third layer), and power factor with respect to the scattering time (last layer), as a function of chemical potential of WN_6 along *xx* (left column) and *zz* (right column) directions at different temperatures.

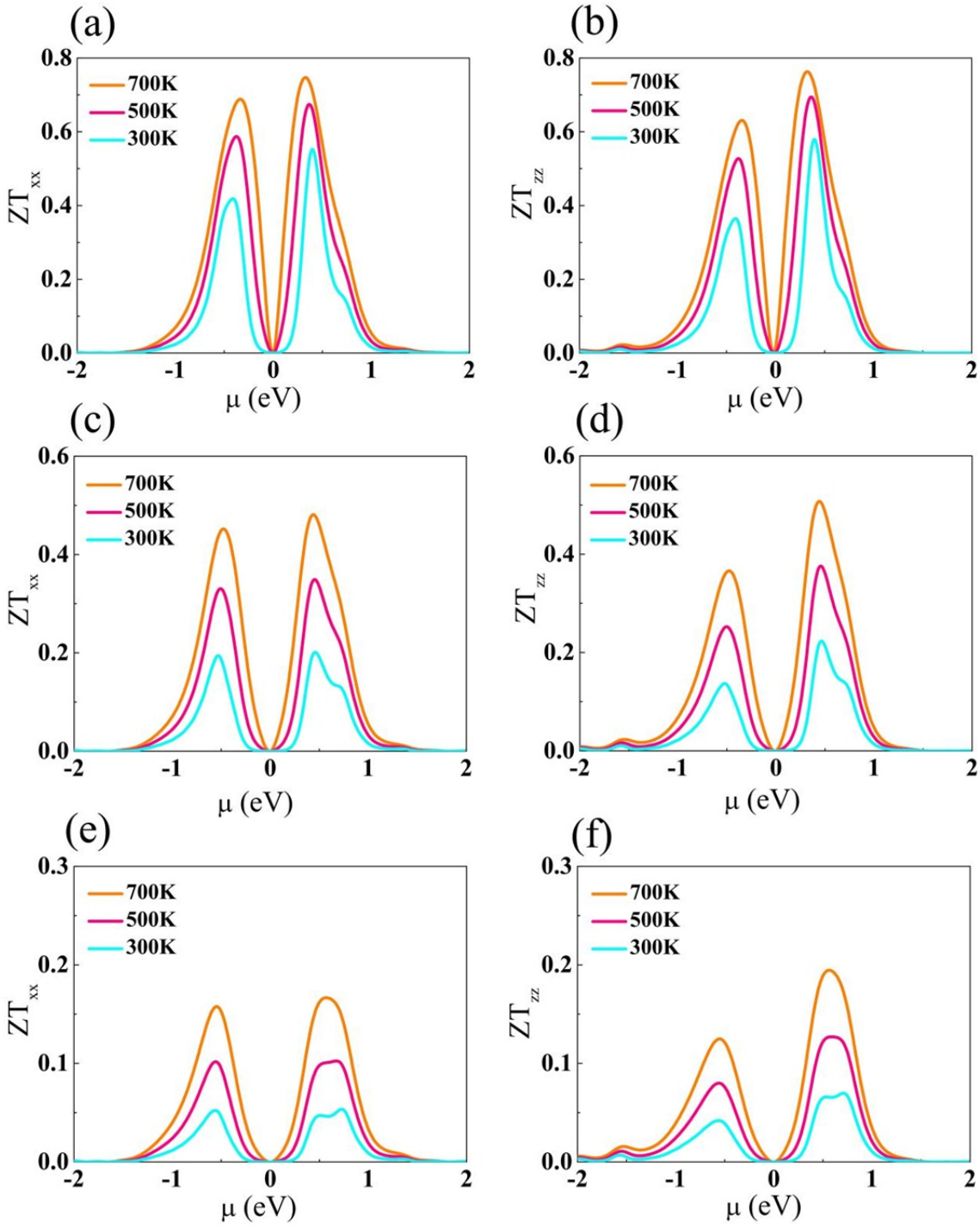

Fig. 5 Figure of merit as a function of chemical potential along the *xx* direction (left panels) and *zz* direction (right panels) with the scattering time τ being 1×10^{-12} s **(a, b)**, 1×10^{-13} s **(c, d)** and 1×10^{-14} s **(e, f)**.

owns analogous curves and weakly anisotropic. The κ_e gradually increases along with varying the absolute value of the chemical potential from the Fermi energy level (μ=0). Based on the Seebeck coefficients and the electrical conductivity, we calculate the $S^2\sigma/\tau$ and present them in Figs. 4g and 4h. The peaks of the $S^2\sigma/\tau$ curves for p-type along the *xx* direction are higher than that along the *zz* direction, while the peaks of n-type along *xx* direction are lower than that along the *zz* direction. By analyzing the power factor, the WN_6 can be categorized as an n-type thermoelectric material.

3.4 Thermoelectric figure of merit

To further intuitively evaluate the thermoelectric properties of WN_6, we calculate its *ZT*. However, calculating scattering time τ is extremely difficult because the complexity scattering mechanisms influence each other. Based on the scattering time value of 1.6×10^{-13} s in WSe_2[7], to attain possible *ZT*, we also select some typical values of the scattering time τ. We use τ=1×10^{-12}, 1×10^{-13} and 1×10^{-14} s in calculating the *ZT* and present the results in Fig. 5. We can see two peaks in the chemical potential range of -1.0 to 1.0 eV. One is in n-type and another in p-type.

Table 1 The scattering time and peak figure merit of WN_6 along *xx* and *zz* directions at 700 K.

	xx crystal direction		*zz* crystal direction	
τ (s)	*ZT* (n)	*ZT* (p)	*ZT* (n)	*ZT* (p)
1×10^{-12}	0.77	0.69	0.78	0.62
1×10^{-13}	0.49	0.45	0.51	0.38
1×10^{-14}	0.17	0.16	0.19	0.13

The crystalline anisotropic of the *ZT* is not that visible. The *ZT* of the n-type is larger than that of the p-type. This is mainly due to the difference of the power factor as shown in Figs. 4g and 4h. Meanwhile, the comparison of the maximum *ZT* of the n-type and p-type at different scattering times are summarized in Table 1. According to Fig. 5 and Table 1, no matter what kinds of scattering time, the *ZT* of the n-type along *zz* direction is always larger than that along *xx* direction, while *ZT* of the p-type along *xx* direction is always larger than that along *zz* direction. These exhibitions directly correlate to electrical conductivity as shown in Figs. 4c and 4d. The highest peaks of the *ZT* curves along *zz* direction are about 0.78, 0.51 and 0.19 with scattering times of 1×10^{-12}, 1×10^{-13} and 1×10^{-14} s, respectively. Overall, our results indicate that the n-type WN_6 is a promising candidate for thermoelectric materials.

4. Conclusion

In summary, we have systematically investigated the phonon and electron transport properties of WN_6, through using DFT and Boltzmann transport methods. Results show that the WN_6 possesses intrinsically relatively low phonon transport ability. The lattice thermal conductivities are about 26.4 and 29.6 W/mk at room temperature along the *xx* and *zz* directions, respectively. This mainly originates from the small phonon group velocity and the strong phonon-phonon scattering. The mode Grüneisen parameters and phonon mean free path are presented to evaluate the anharmonic properties and the size effects. Similar to the thermal conductivity, the Seeback coefficients and electrical conductivity present weak anisotropic behaviors. A large Seeback coefficient can approach 1330 μV/K. The power factor indicates that WN_6 is an n-type thermoelectric material. The maximum *ZT* of WN_6 can be 0.78 at 700 K for n-type along *zz* direction. Our results provide reasonable theoretical foundation for further experiments.

Conflicts of interest

There are no conflicts to declare.

Acknowledgements

The calculations were performed at the Supercomputer Centre in the China Spallation Neutron Source. This work was financially supported by National Natural Science Foundation of China (NSFC) (Grant No. 11874145) and Guangdong Provincial Department of Science and Technology, China (No. 2018A0303100013).

References

1. S. Chu, Y. Cui and N. Liu, *Nat. Mater.*, 2017, **16**, 16.
2. M. Aneke and M. Wang, *Appl. Energy*, 2016, **179**, 350-377.
3. J. Wang, F. Xie, X. H. Cao, S. C. An, W. X. Zhou, L. M. Tang and K. Q. Chen, *Sci. Rep*., 2017, **7**, 41418.
4. Y. Pei, H. Wang and G. J. Snyder, *Adv. Mater*., 2012, **24**, 6125-6135.
5. D. Champier, *Energy Convers. Manage*., 2017, **140**, 167-181.
6. C. Meng, C. Liu and S. Fan, *Adv. Mater*., 2010, **22**, 535-539.
7. S. Kumar and U. Schwingenschlögl, *Chem. Mater*., 2015, **27**, 1278-1284.
8. J. Yang, L. X, J. Qiu, L. Wu, X. Shi, L. Chen, J. Yang, W. Zhang and C. Uher, J. David, *npj Comput. Mater*., 2016, **2**, 15015.
9. J. M. Skelton, S. C. Parker, A. Togo, I. Tanaka and A. Walsh, *Phys. Rev. B*, 2014, **89**, 205203.
10. C. M. Jaworski, B. Wiendlocha, V. Jovovic and J. P. Heremans, *Energ. Environ. Sci*., 2011, **4**, 4155-4162.
11. D. Xie, B. Zhang, A. Zhang, Y. Chen, Y. Yan, H. Yang, G. Wang, G. Wang, X. Han, G. Han, X. Lu and X. Zhou, *Nanoscale*, 2018, **10**, 14546-1455.
12. T. Ouyang, E. L. Jiang, C. Tang, J. Li, C. Y. He and J. X. Zhong, *J. Mater. Chem. A*, 2018, **6**, 21532.
13. W. X. Zhou and K. Q. Chen, *Carbon*, 2015, **85**, 24-27.
14. L. D. Zhao, S. H. Lo, Y. Zhang, H. Sun, G. Tan, C. Uher, C. Wolverton, V. P. Dravid and M. G. Kanatzidis, *Nature*, 2014, **508**, 373.
15. B. L. Li and K. Q. Chen, *Carbon*, 2017, **119**, 548-554.
16. Y. Zhao, L. Yang, L. Kong, M. H. Nai, D. Liu, J. Wu, Y. Liu, S.Y. Chiam, W. K. Chim, C. T. Lim, B. Li, J. T. L. Thong and K. Hippalgaonkar, *Adv. Funct. Mater*., 2017, **27**, 1702824.
17. Z. Wang, L. Zhao, K. F. Mak and J. Shan, *Nano Lett*., 2017, **17**, 740-746.
18. J. H. Bahk and A. Shakouri, *Appl. Phys. Lett*., 2014, **105**, 052106.
19. A. Cupo and V. Meunier, *J. Phys.: Condens. Matter*., 2017, **29**, 283001.
20. J. Hansson, T. M. J. Nilsson, L. Ye and J. Liu, *Int. Mat. Rev*., 2018, **63**, 22-45.
21. N. Zen, T. A. Puurtinen, T. J. Isotalo, S. Chaudhuri and I. J. Maasilta, *Nat. Commun*., 2014, **5**, 3435.
22. X. Y. Mi, X. Yu, K. L. Yao, X. Huang, N. Yang and J. T. Lü, *Nano Lett*., 2015, **15**, 5229-5234.
23. L. Yang, N. Yang and B. Li, *Nano Lett.*, 2014, **14**, 1734-1738.
24. L. Yang, N. Yang and B. Li, *Sci. Rep*., 2013, **3**, 1143.
25. L. D. Zhao, S. H. Lo, Y. Zhang, H. Sun, G. Tan, C. Uher, C. Wolverton and V. P. Dravid, *Nature*, 2014, **508**, 373.
26. Y. Min, J. W. Roh, H. Yang, M. Park, S. Kim, S. Hwang, S. M. Lee, K. H. Lee and U. Jeong, *Adv. Matter*., 2013, **25**, 1425-1429.
27. Q. Yan, H. Chen, W. Zhou, H. H. Hng, F. Y. C. Boey and J. Ma, *Chem. Mater*., 2008, **20**, 6298-6300.
28. J. Androulakis, Y. Lee and I. Todorov, *Phys. Rev. B*, 2011, **83**, 195209.
29. S. K. Bux, M. T. Yeung, E. S. Toberer, G. J. Snyder, R. B. Kaner and J. P. Fleurial, *J. Mater. Chem*., 2011, **21**, 12259-1226.
30. G. Rogl, A. Grytsiv, P. Rogl, N. Peranio, E. Bauer, M. Zehetbauer and O. Eibl, *Acta. Mater*., 2014, **63**, 30-43.
31. H. Kleinke, *Chem. Mater*., 2009, **22**, 604-611.

32. Y. He, T. Day, T. Zhang, H. Liu, X. Shi, L. Chen and G. J. Snyder, *Adv. Mater*., 2014, **26**, 3974-3978.
33. P. Eklund, S. Kerdsongpanya and B. Alling, *J. Mater. Chem C*, 2016, **4**, 3905-3914.
34. C. X. Quintela, J. P. Podkaminer, M. N. Luckyanova, T. R. Paudel, E. L. Thies, D. A. Hillsberry, D. A. Tenne, E. Y Tsymbal, G. Chen, C. B. Eom and F. Rivadulla, *Adv. Mater*., 2015, **27**, 3032-3037.
35. M. J. Mehl, D. Finkenstadt, C. Dane, G. L. W. Hart and S. Curarolo, *Phys. Rev. B*, 2015, **91**, 184110.
36. Lu C, Li Q, Ma Y and C. Chen, *Phys. Rev. Lett*., 2017, **119**, 115503.
37. K. Xia, H. Gao, C. Liu, J. Yuan, J. Sun, H. T. Wang and D. Xing, *Sci. Bull.*, 2018, **63**, 817-824.
38. G. Kresse and J. Furthmüller, *Phys. Rev. B*, 1996, **54**, 11169–11186.
39. J. P. Perdew, K. Burke and M. Ernzerhof, *Phys. Rev. Lett*., 1996, **77**, 3865.
40. W. Li, J. Carrete, N. A. Katcho and N. Mingo, *Comput. Phys. Commun*., 2014, **185**, 1747-1758.
41. A. Togo, F. Oba and I. Tanaka, *Phys. Rev. B*, 2008, **78**, 134106.
42. W. Li, L. Lindsay, D. A. Broido, D. A. Stewart and N. Mingo, *Phys. Rev. B*, 2012, **86**, 174307.
43. G. K. H. Madsen and D. J. Singh, *Comput. Phys. Commun*., 2006, **175**, 67–71.
44. J. Yang, H. Li, T. Wu, W. Zhang, L. Chen and J. Yang, *Adv. Funct. Mater*., 2008, **18**, 2880-2888.
45. B. T. Wang, M. A. Petrukhina and E. R. Margine, *Carbon*, 2015, **94**, 174-180.
46. D. Parker and D. J. Singh. *J. Appl. Phys*., 2010, **108**, 083712.
47. Y. L. Yan and Y. X. Wang. *J. Mater. Chem*., 2011, **21**, 12497-12502.
48. M. S. Lee, F. P. Poudeu and S. D. Mahanti. *Phys. Rev. B*, 2011, **83**, 085204.
49. C. Fu, H. Wu, Y. Liu, J. He, X. Zhao and T. Zhu, *Adv. Sci*., 2016, **3**, 1600035.
50. D. Parker, and D. J. Singh. *Phys. Rev. B*, 2012, **85**, 125209.
51. M. Zhou, Z. M. Gibbs, H. Wang, Y. Han, C. Xin, L. Li and G. J. Snyder, *Phys. Chem. Chem. Phys*., 2014, **16**, 20741-20748.
52. W. Li, N. Mingo, L. Lindsay, D. A. Broido, D. A. Stewart and N. A. Katcho, *Phys. Rev. B*, 2012, **85**, 195436.
53. A. I. Hochbaum, R. Chen, R. D. Delgado, W. Liang, E. C. Garnett, M. Najarian, A. Majumdar and P. Yang, *Nature*, 2008, **451**, 163-168.
54. W. X. Zhou and K. Q. Chen, *Sci. Rep*., 2014, **4**, 7150.
55. C. X. Yu, G. Zhang, Y. W. Zhang and L. M. Peng, *Nano Energy*, 2015, **17**, 104-110.
56. J. W. Lim, H. T. Wang, J. Y. Tang, S. C. Andrews, H. Y. So, J. Lee, D. H. Lee, T. P. Russell and P. D. Yang, *ACS Nano*, 2016, **10**, 124-132.
57. G. F. Xie, Z. F. Ju, K. K. Zhou, X. L. Wei, Z. X. Guo, Y. Q. Cai and G. Zhang, *npj Comput. Mater*., 2018, **4**, 21.
58. T. Markussen, A. P. Jauho and M. Brandbyge, *Phys. Rev. Lett*., 2009, **103**, 055502.
59. Y. Y. Liu, Y. J. Zeng, P. Z. Jia, X. H. Cao, X. W. Jiang and K. Q. Chen, *J. Phys.: Condens. Matter*., 2018, **30**, 275701.
60. G. F. Xie, D. Ding and G. Zhang, *Adv. Phys. X*, 2018, **3**, 1480417.
61. D. F. Li, J. He, G. Q. Ding, Q. Q. Tang, Y. Ying, J. j. He, C. Y. Zhong, Y. Liu, C. B. Feng, Q. L. Sun, H. B. Zhou, P. Zhou and G. Zhang. *Adv. Func. Mater*., 2018, 1801685.
62. A. J. Minnich, J. A. Johnson, A. J. Schmidt, K. Esfarjani, M. S. Dresselhaus, K. A. Nelson and G. Chen, *Phys. Rev. Lett*., 2011, **107**, 095901.
63. G. F. Xie, Y. Guo, X. L. Wei, K. W. Zhang, L. Z. Sun, J. X. Zhong, G. Zhang and Y. W. Zhang, *Appl. Phys. Lett*., 2014, **104**, 233901.
64. G. F. Xie and Y. L. Shen, *Phys. Chem. Chem. Phys*., 2015, **17**, 8822-8827.
65. D. Ma, H. Ding, H. Meng, L. Feng, Y. Wu, J. Shiomi and N. Yang, *Phys. Rev. B*, 2016, **94**, 165434.
66. H. Bao, J. Chen, X. K. Gu and B. Y. Cao, *ES Energy Environ.*, 2018, **1**, 16-55.
67. S. Yabuuchi, M. Okamoto, A. Nishide, Y. Kurosaki and J. Hayakawa, *Appl. Phys. Express*, 2013, **6**, 025504.
68. L. Yang, N. Yang and B. Li, *Int. J. Heat Mass Transfer*, 2016, **99**, 102-106.
69. G. Wiedemann and R. Franz, *Ann. Phys*., 1853, **89**, 497-531.